

Model-based target decomposition with the $\pi/4$ mode compact polarimetry data

Shenglong GUO^{1,2}, Yang LI^{1,2}, Wen HONG^{1*},
Jianfeng WANG^{1,2} & Xiaoyang GUO^{1,2}

¹*Institute of Electronics, Chinese Academy of Sciences, Beijing 100190, China;*

²*School of Electronics, Electrical and Communication Engineering,
University of Chinese Academy of Sciences, Beijing 100190, China*

Received May 27, 2015; accepted August 26, 2015; published online April 13, 2016

Abstract In this paper, model-based (surface, dihedral and volume scattering) target decomposition technique is proposed to decompose the $\pi/4$ mode compact polarimetric radar data. A general relationship between fully polarimetric coherence matrix and the Stokes vector of the $\pi/4$ mode compact polarimetric data is first established. Based on the Stokes vector, a proposed algorithm to retrieve the power of three scattering mechanisms is given in details. We validate this algorithm with L-band AIRSAR, San Francisco Bay, and results of decomposition are discussed and assessed in detail by being compared with the quad-pol Freeman-Durden decomposition results. Finally, the $\pi/4$ mode decomposition is compared with the CTRLR (circular transmitting and linear receiving) mode, and with the $\pi/4$ mode $m - \delta$ targets decomposition. The comparison results are analyzed and discussed in detail.

Keywords $\pi/4$ mode compact polarimetry, mode-based target decomposition, Stokes vector, RVoG model, radar polarimetry

Citation Guo S L, Li Y, Hong W, et al. Model-based target decomposition with the $\pi/4$ mode compact polarimetry data. *Sci China Inf Sci*, 2016, 59(6): 062307, doi: 10.1007/s11432-015-5478-4

1 Introduction

In recent years, there have emerged new SAR modes based on the transmission of polarization states rather than the canonical H and V polarizations. Among the infinite combinations of transmit and receive polarizations, three special classes have been considered [1]. The first class is called $\pi/4$ mode compact polarimetry, and denotes a variant of current dual polarimetric modes having a combination of polarization H and V (linear polarization oriented at 45°) in transmission and the coherent H, V in reception [2]. The second one is named the CTRLR mode compact polarimetry [3,4], where the transmission is circular and the reception is linear. The third class of SAR architectures is the dual circular polarimetric mode [5] (the CC mode), whose peculiarity is the transmission and reception at circularly polarized states.

In this paper, we mainly focus on the $\pi/4$ mode, where the transmission of linearly polarized wave is oriented at 45° and the reception wave is H-, V-polarized. The $\pi/4$ mode compact-pol electric vector of the backscattered field can be projected from the quad-pol complex scattering matrix as shown in [3],

* Corresponding author (email: wendy_hong@163.com)

$$\begin{bmatrix} E_{HL} \\ E_{VL} \end{bmatrix} = \begin{bmatrix} S_{HH} & S_{HV} \\ S_{VH} & S_{VV} \end{bmatrix} \frac{1}{\sqrt{2}} \begin{bmatrix} 1 \\ \pm 1 \end{bmatrix} = \frac{1}{\sqrt{2}} \begin{bmatrix} S_{HH} \pm S_{HV} \\ S_{VH} \pm S_{VV} \end{bmatrix}, \quad (1)$$

where the + sign is for +45° linear polarization transmit and the – sign is for –45° linear polarization transmit. Here, E is the (complex) voltage in the subscripted polarization. The subscript HL means the linear-polarization transmission and H-pol reception. Similarly, VL stands for linear-pol transmission and V-pol reception. The factor $\sqrt{2}$ accounts for 3 dB budget loss in the radar output with respect to classical dual or full polarimetric modes [2].

Lots of analyses of compact polarimetry are based on the four-element real Stokes vector (SV) [6] of the scattered wave [7, 8]. To retrieve the SV, the 2×2 average wave coherency matrix \mathbf{J}_2 should be derived firstly, as defined in

$$\mathbf{J}_2 = \begin{bmatrix} \langle E_{HL} E_{HL}^* \rangle & \langle E_{HL} E_{VL}^* \rangle \\ \langle E_{VL} E_{HL}^* \rangle & \langle E_{VL} E_{VL}^* \rangle \end{bmatrix} = \frac{1}{2} \begin{bmatrix} g_0 + g_1 & g_2 - jg_3 \\ g_2 + jg_3 & g_0 - g_1 \end{bmatrix}. \quad (2)$$

In above expressions, * denotes complex conjugate, $\langle \dots \rangle$ denotes averaging. For scattering wave, the four elements of the SV must satisfy the following inequality:

$$g_0^2 \geq \sum_{i=1}^3 g_i^2. \quad (3)$$

In particular, when the equality holds, it's corresponding to a completely polarized wave, and when $\sum_{i=1}^3 g_i^2 = 0$, it is corresponding to a completely depolarized wave. Consequently a well-known wave decomposition theorem [9] is shown in

$$\underline{g} = \underline{g}_n + \underline{g}_p = \begin{bmatrix} g_{0n} \\ 0 \\ 0 \\ 0 \end{bmatrix} + \begin{bmatrix} g_{0p} \\ g_1 \\ g_2 \\ g_3 \end{bmatrix} \Rightarrow g_{0p}^2 = \sum_{i=1}^3 g_i^2, \quad (4)$$

which allows us to consider an arbitrary wave as the sum of a noise signal and a completely polarized wave.

This is the basis of the $m - \delta$ classification [3], which has been successfully applied to a range of applications in [3, 7, 8, 10]. Here, m is the degree of polarization, and δ is the relative phase. These two parameters are defined as

$$m = \frac{1}{g_0} \sqrt{\sum_{i=1}^3 g_i^2} \quad \delta = \tan^{-1} \left(\frac{g_2}{g_3} \right). \quad (5)$$

Note that, expression of δ in $\pi/4$ mode is different from that in the CTLR mode where g_3 is in the numerator and g_2 is in the denominator.

All above are well-known features of compact polarimetry [2, 10]. In this paper, we will extend the analysis on the SV of the $\pi/4$ mode to test the target decomposition [11] ability of the $\pi/4$ mode compact-pol data. This is very significant in that target decomposition is the foundation of target classification and further applications.

The $m - \delta$ decomposition is the existing decomposition technique for the $\pi/4$ mode and the CTLR mode compact PolSAR data [7]. However, this decomposition has some shortcomings which bring decomposition errors. The m estimation which corresponds to the volume scattering is not accurate. What's more, δ is indeed a function of the surface and dihedral scattering mechanisms, but it not only depends on scattering mechanisms. It also depends on a useless phase, which is undesirable. In this paper, we will propose a new method: model-based target decomposition. The proposed method can retrieve a parameter which only depends on the surface and dihedral scattering mechanisms. As a result, the proposed decomposition method will overcome the above disadvantages. In this paper, we will construct a

general link between quad-pol coherence matrix and the corresponding SV. Further, the $\pi/4$ mode SV of the random volume scattering and the rank-1 pure scattering mechanism (which means that the rank of scattering matrix is one) are obtained. Finally, the $\pi/4$ mode random volume over ground (RVoG) model is constructed. Based on the SV of the RVoG model, we will apply model-based target decomposition technique to the $\pi/4$ mode compact-pol data. Since the SV roots in the quad-pol coherence matrix, the decomposition results can be compared with that of the quad-pol model-based target decomposition.

This paper is organized as follows. In Section 2, Model-based decomposition approach will be introduced. Decomposition results are presented and analyzed in Section 3 with L-band AIRSAR, San Francisco Bay. Conclusion is set out in Section 4.

2 Model-based target decomposition

In this section, we will deduce the approach of model-based target decomposition with $\pi/4$ mode compact-pol data. We first make a general link between the SV and the quad-pol 3×3 scattering coherency matrix. Then we will deduce the SV respectively corresponding to the random volume scattering mechanism and the pure scattering mechanism specifically. Lastly, the Stokes vector of the RVoG model is built, and the decomposition approach is developed.

2.1 Mapping the $\pi/4$ mode compact-pol SV to T_3

To find the link between the compact-pol SV and T_3 , we rewrite (1) as

$$\begin{bmatrix} E_{HL} \\ E_{VL} \end{bmatrix} = \frac{1}{2} \begin{bmatrix} 1 & 1 & \pm 1 \\ \pm 1 & \mp 1 & 1 \end{bmatrix} \underline{k}, \quad (6)$$

wherein \underline{k} is the quad-pol target vector in the Pauli basis. In (6), the upper and lower signs stand for 45° and -45° polarizations, respectively.

Based on (2), the 2×2 compact-pol coherency matrix J_2 can be expressed as

$$J_2 = \frac{1}{4} \begin{bmatrix} 1 & 1 & \pm 1 \\ \pm 1 & \mp 1 & 1 \end{bmatrix} T_3 \begin{bmatrix} 1 & 1 & \pm 1 \\ \pm 1 & \mp 1 & 1 \end{bmatrix}^T = \frac{1}{2} \begin{bmatrix} g_0 + g_1 & g_2 - jg_3 \\ g_2 + jg_3 & g_0 - g_1 \end{bmatrix}, \quad (7)$$

where T means matrix transposition.

Finally, the SV can be obtained

$$T_3 = \begin{bmatrix} t_{11} & t_{12} & t_{13} \\ t_{12}^* & t_{22} & t_{23} \\ t_{13}^* & t_{23}^* & t_{33} \end{bmatrix} \rightarrow \underline{g} = \begin{bmatrix} g_0 \\ g_1 \\ g_2 \\ g_3 \end{bmatrix} = \begin{bmatrix} \frac{1}{2}(t_{11} + t_{22} + t_{33}) \pm \text{Re}(t_{13}) \\ \text{Re}(t_{12}) \pm \text{Re}(t_{23}) \\ \pm \frac{1}{2}(t_{11} - t_{22} + t_{33}) + \text{Re}(t_{13}) \\ \pm \text{Im}(t_{12}) - \text{Im}(t_{23}) \end{bmatrix}, \quad (8)$$

Re and Im stand for the real and the imaginary value of the complex amplitude, respectively.

A common approximation in model-based decompositions is to assume a priori that T_3 has the reflection symmetric form ($t_{13} = t_{23} = 0$) in (9) [12]. Consequently, this reflection symmetry in compact polarimetry leads to a simplified SV, as shown in

$$T_3 = \begin{bmatrix} t_{11} & t_{12} & 0 \\ t_{12}^* & t_{22} & 0 \\ 0 & 0 & t_{33} \end{bmatrix} \rightarrow \underline{g} = \begin{bmatrix} g_0 \\ g_1 \\ g_2 \\ g_3 \end{bmatrix} = \begin{bmatrix} \frac{1}{2}(t_{11} + t_{22} + t_{33}) \\ \text{Re}(t_{12}) \\ \pm \frac{1}{2}(t_{11} - t_{22} + t_{33}) \\ \pm \text{Im}(t_{12}) \end{bmatrix} \Rightarrow \begin{cases} \text{span} = 2g_0, \\ t_{12} = g_1 \pm jg_3, \\ t_{22} = g_0 \mp g_2. \end{cases} \quad (9)$$

Under this assumption, we see that, with the $\pi/4$ mode compact system, we can estimate the span of T_3 , the complex element t_{12} , and the second Pauli element t_{22} . We can also determine the sum $t_{11} + t_{33}$, but unfortunately not the two separately.

2.2 Compact SV of the pure scattering mechanism

One important decomposition approach in the quad-pol SAR is H/α decomposition [12,13], which is based on the eigenvector analysis of \mathbf{T}_3 . Here, a key physical parameter is α , which identifies the scattering mechanism in the range $0 \leq \alpha \leq 90^\circ$ ($\alpha = 0$ for the surface scattering, $\alpha = 90^\circ$ for the double-bounce scattering). In this section, we relate this parameter to the compact SV.

Consider a general rank-1 symmetric scattering mechanism with a \mathbf{T}_3 matrix, as shown in (10). According to (9), it is very easy to obtain the compact SV as shown in

$$\mathbf{T}_3 = m_p \begin{bmatrix} \cos^2 \alpha & \cos \alpha \sin \alpha e^{j\varphi} & 0 \\ \cos \alpha \sin \alpha e^{-j\varphi} & \sin^2 \alpha & 0 \\ 0 & 0 & 0 \end{bmatrix} \rightarrow \underline{g}_p = \frac{m_p}{2} \begin{bmatrix} 1 \\ \sin 2\alpha \cos \varphi \\ \pm \cos 2\alpha \\ \pm \sin 2\alpha \sin \varphi \end{bmatrix}. \quad (10)$$

According to (10), it obviously shows that, we can obtain an estimate of both target parameters α and φ from $\pi/4$ mode compact data, as shown in the following equation:

$$\alpha = \frac{1}{2} \tan^{-1} \left(\frac{\sqrt{g_1^2 + g_3^2}}{\pm g_2} \right), \quad \varphi = \arg(g_1 \pm jg_3). \quad (11)$$

In (11), $\alpha = 0$ is for the pure surface scattering, and $\alpha = 90^\circ$ for the pure double scattering.

2.3 Compact SV of the random volume scattering

Considering that volume scattering is formed by a cloud of anisotropic particles (of arbitrary electrical size) but with azimuthal symmetry in the cloud, the volume scattering matrix is shown in

$$\mathbf{T}_3 = m_v \begin{bmatrix} F_p & 0 & 0 \\ 0 & 1 & 0 \\ 0 & 0 & 1 \end{bmatrix} \rightarrow \underline{g}_v = \frac{m_v}{2} \begin{bmatrix} 2 + F_p \\ 0 \\ \pm F_p \\ 0 \end{bmatrix}, \quad (12)$$

where F_p is a mean particle shape parameter in the volume [14]. In this case, we all call it as the random volume scattering.

The SV of the random volume scattering can be retrieved as shown in (12). In general, we see that the volume is a mixture of a pure scattering mechanism and a noise signal. A common situation in practice is that the volume scattering consists of dipole clouds, which is widely used in the Freeman-Durden decomposition. In this case, $F_p = 2$. Eq. (12) can be expressed as

$$\underline{g}_v = 2m_v [1 \ 0 \ \pm 0.5 \ 0]^T. \quad (13)$$

We note that the SV of the random volume scattering in the $\pi/4$ mode is quite different from the CTLR mode, where the SV of the random volume scattering is shown in (see [15])

$$\underline{g}_v = 2m_v [1 \ 0 \ 0 \ 0]^T. \quad (14)$$

By contrast, we find that in the $\pi/4$ mode the volume scattering is not a complete noise signal. Instead, it can be divided into a pure noise signal and a fully polarized wave.

2.4 Three-component compact decomposition

To decompose the compact-pol power into three components power respectively corresponding to the surface scattering P_S , the dihedral scattering P_D , and the random volume scattering P_V , we first build

the RVoG model by combining the pure scattering mechanism with the random volume mode. In the following, we will only analyze the $+45^\circ$ linear-polarization transmission $\pi/4$ mode. The compact-pol SV of the RVoG model [16] is defined as

$$\underline{g} = 2m_v \begin{bmatrix} 1 \\ 0 \\ 0.5 \\ 0 \end{bmatrix} + m_p \begin{bmatrix} 1 \\ \sin 2\alpha \cos \varphi \\ \cos 2\alpha \\ \sin 2\alpha \sin \varphi \end{bmatrix}, \quad (15)$$

where m_p is equal to the term $m_p/2$ in (10). In order to facilitate the expression, we omit the factor $1/2$.

Note that in (15), the volume component is not a completely depolarized noise signal. We could not estimate the m_v by the traditional method: $m_v = g_0(1 - m)$ [17]. A new method should be considered as follows.

Three new variables a, b, c are introduced to take the places of the three terms: $\sin 2\alpha \cos \varphi$, $\cos 2\alpha$, and $\sin 2\alpha \sin \varphi$, respectively. Note that this model has four observables (the SV) and five unknowns: m_v, m_p, a, b, c , and the unknowns seemingly cannot be inverted from the compact data without further model assumptions. However, there is another constrain relation, i.e., $a^2 + b^2 + c^2 = 1$. As a result, equations can be developed as shown in (16) and they have analytical solutions:

$$\begin{cases} 2m_v + m_p = g_0, & (16a) \\ m_p a = g_1, & (16b) \\ m_v + m_p b = g_2, & (16c) \\ m_p c = g_3, & (16d) \\ a^2 + b^2 + c^2 = 1. & (16e) \end{cases}$$

Detailed steps to solve (16) are shown in the following items:

- Based on (16b) and (16d), we define $t = g_1/g_3$. As a result, the relation $a = ct$ can be got;
- According to (16b), $m_p = g_1/a = g_1/(ct)$;
- Then referring to (16a), we get $m_v = (g_0 - m_p)/2$;
- According to (16c), b can be expressed by the function of ct , deduced as $b = (g_2 - m_v)/m_p = (g_2/g_1 - g_0/(2g_1))ct + 0.5$;
- Substitute a, b, c into (16e), and parameter c can be estimated;
- Once obtaining c , based on the relations shown in the above steps, we can estimate a, b, m_p , and m_v .

This algorithm represents decomposition into a pure (rank-1) scattering mechanism and the volume scattering. Next, we will further decompose the pure scattering power into the surface and the dihedral scattering components.

As we know, the parameter α which can be estimated by (17) in (15) decides the scattering mechanism belonging to the surface scattering or the dihedral scattering. $\alpha = 0$ stands for the surface scattering, and $\alpha = 90^\circ$ for the dihedral scattering. However, if $0 < \alpha < 90^\circ$, it contains both the surface and dihedral scattering components. In this case, the single-component power is effectively split into two to represent the dihedral and surface components using a geometrical factor $(1 \pm \cos 2\alpha)$ [15]. Finally, the model-based decomposition components can be retrieved in (18).

$$\alpha = \frac{1}{2} \tan^{-1} \left(\frac{\sqrt{a^2 + c^2}}{\pm b} \right). \quad (17)$$

$$\begin{cases} P_S = 0.5m_p(1 + \cos 2\alpha), \\ P_D = 0.5m_p(1 - \cos 2\alpha), \\ P_V = 2m_v. \end{cases} \quad (18)$$

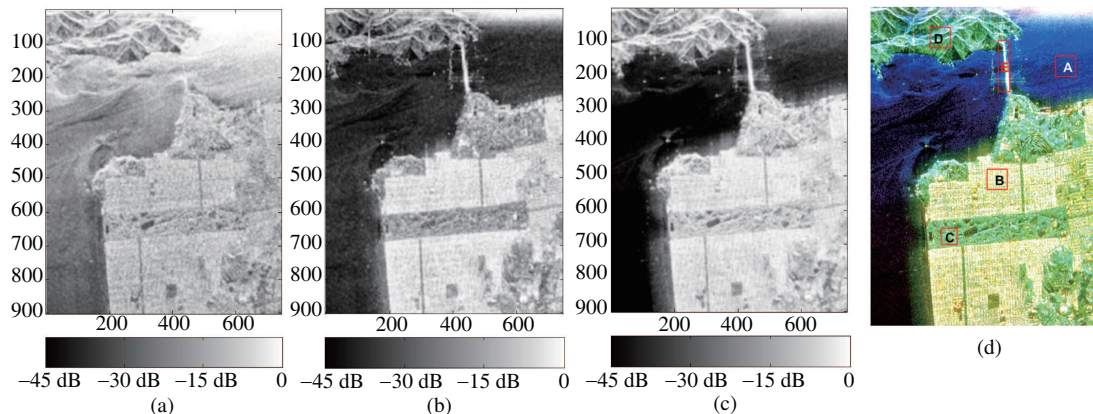


Figure 1 (Color online) Scattering mechanisms contributions reconstructed after the model-based target decomposition: (a) surface scattering; (b) double-bounce scattering; (c) volume scattering; and (d) color coded image of this decomposition.

3 Experiment results

In this paper, we apply the model-based target decomposition technique (which has been already given in Section 2) to decompose the $\pi/4$ mode compact-pol data and analyze the decomposition results. According to decomposition results, we demonstrate the preservation of scattering mechanism information in $\pi/4$ mode compact-pol data. At last, we compare the decomposition results of the $\pi/4$ mode compact-pol data with the CTLR mode hybrid-pol data.

3.1 Decomposition for the San Francisco Bay area

National Aeronautics and Space Administration/Jet Propulsion Laboratory Airborne Synthetic Aperture Radar (Airsar) L-band data of San Francisco Bay, CA, is used in this section. This classic fully polarimetric SAR data provides a good coverage of typical targets such as the ocean, buildings, trees, beaches, bridges and so on. Note that the AirSAR data is full PolSAR data, we should first transform it to $\pi/4$ mode compact PolSAR data according to (1). Then the model-based target decomposition technique is applied to decompose the compact PolSAR data.

The model-based target decomposition results are illustrated in Figure 1(a)–(c), and Figure 1(d) presents the corresponding color-coded image. Overall, the decomposition performs very well for its clear classification and coloring (blue, ocean/water; green, trees and mountains with plants; and slight yellow, urban area) of the ground objects. Detailed analysis and discussions will be given next. Here, we first make an interpretation that in Figure 1(d), A is for Ocean; B, Buildings; C, Trees; D, Mountain; E, Bridge.

Estimated scattering power (listed in Table 1) and normalized power of typical targets are respectively shown in Figures 2 and 3. The power of each typical target is the statistical mean value of the corresponding homogenous area. According to Figure 1(a)–(c) and Figure 2(a), for the sea area, the surface scatter is the strongest component in that sea surface is smooth and fits the small perturbation model [11] quite well. The double-bounce and volume scattering are significantly low. The decomposition results closely coincide with quad-pol Freeman-Durden decomposition (see Figure 2(b)), where surface scatter component is significantly higher than the double-bounce and volume scatter component. In addition, except the dihedral scattering, the normalized power of the $\pi/4$ mode decomposition is near to that of the quad-pol decomposition as shown in Figure 3. Compared with the quad-pol decomposition, the only difference is the increased double-bounce scattering component of the $\pi/4$ mode decomposition. However, even though the dihedral scattering is raised, it is still much less than the surface scattering (which is dominant as expected) and cannot impact the decomposition results.

For urban area, all the three scattering components are dominant. Since there are many trees and man-made targets that have strong depolarization components, the volume scattering component (regarded

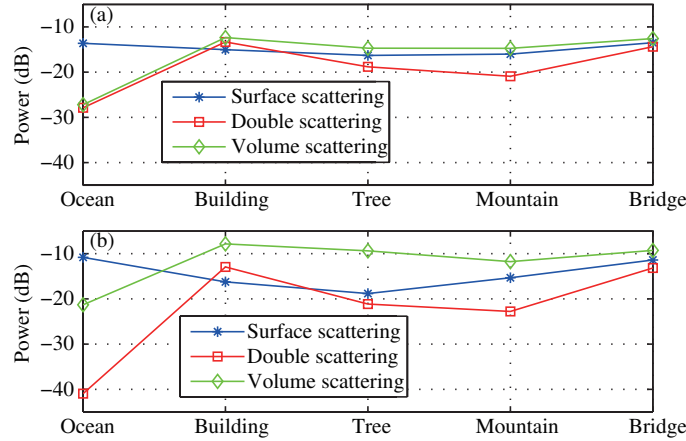


Figure 2 (Color online) Estimated scattering power (a) of the model-based target decomposition of the $\pi/4$ mode compact-pol data, and (b) the Freeman-Durden decomposition of the quad-pol data (dB).

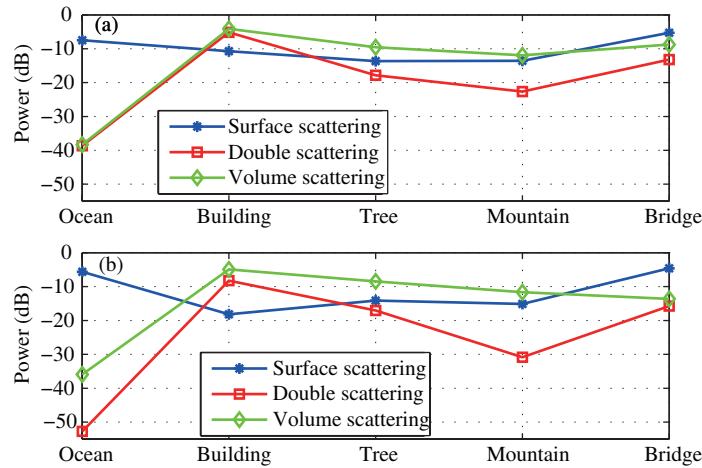


Figure 3 (Color online) Normalized scattering power (a) of the model-based target decomposition of the $\pi/4$ mode compact-pol data, and (b) the Freeman-Durden decomposition of the quad-pol data (dB).

as depolarization component) is strong. Buildings which form a dihedral angle with ground result in high dihedral scattering component. Roofs of buildings and roads have strong surface scattering component. In addition, no matter the normalized power or the non-normalized power, all the three components have the same trend (volume > dihedral > surface scattering) with the quad-pol decomposition referring to Figures 2 and 3.

For tree areas, the volume scatter dominates, which is expected for its strong depolarization ability. The surface scattering is a little less (2 dB) than the volume scatter. The double-bounce scatter is the lowest one. Decomposition results are the same (volume > surface > dihedral scattering) with the quad-pol decomposition referred to in Figures 2 and 3. This decomposition results of forests are different from the CTLR mode decomposition where the double-bounce is higher than the surface scattering. The analysis and reason will be discussed in detail later.

Volume scattering dominates in the mountain area which is filled with meadows and other plants, and the surface scattering is inferior to it. The double scattering is conspicuously low for lacking the dihedral reflection. The decomposition results agree with the quad-pol decomposition very well (referring to Figures 2 and 3). Around the bridge, three scattering powers are all high as shown in Figure 2. This is in agreement with facts that bridge surface results in the strong surface scattering; the dihedral angle between guardrail and bridge surface (water and bridge) accounts for the double-bounce scattering; edge of bridge has the strong volume scattering. However, even though the powers of the dihedral and volume

Table 1 Estimated scattering mechanism contributions for typical targets with different modes and different decomposition methods (dB)

	$\pi/4$			CTLR			$m - \delta$			Quad-pol		
	Ps	Pd	Pv	Ps	Pd	Pv	Ps	Pd	Pv	Ps	Pd	Pv
Ocean	-13.6	-27.9	-27.2	-13.8	-27.8	-25.6	-18.7	-24.9	-29.8	-10.8	-40.9	-21.3
Buildings	-15.0	-13.3	-12.3	-15.5	-13.0	-12.8	-13.9	-14.7	-12.3	-16.2	-12.9	-7.9
Trees*	-16.3	-18.8	-14.7	-18.2	-16.7	-14.7	-16.1	-17.3	-15.7	-18.8	-21.4	-9.4
Mountain*	-15.8	-20.9	-14.5	-16.9	-19.4	-15.2	-16.7	-17.8	-17.0	-15.3	-22.7	-10.8
Bridge	-13.4	-14.3	-12.6	-13.5	-14.1	-12.9	-13.6	-14.5	-13.0	-11.4	-13.1	-9.3

scattering components are stronger, their normalized powers are not as strong as the surface scattering. That is because, in the whole channel, urban region has the strongest dihedral scattering component and the strongest volume scattering component.

Finally, we must note that the dominant scattering components of different targets with the $\pi/4$ mode decomposition are all about 3 dB less than the quad-pol decomposition due to the 3 dB loss (as mentioned in Section 1) when projecting quad-pol to compact-pol. In contrast with the quad-pol decomposition results, we know that much of the scattering mechanism information is preserved in the $\pi/4$ mode compact-pol data.

3.2 Comparison of $\pi/4$ and CTLR mode

In this section, we will make a comparison between the $\pi/4$ mode and the CTLR mode model-based decomposition. The decomposition powers of the three scattering mechanisms are listed in Table 1.

According to Table 1, except Trees* and Mountain*, two compact-pol modes have the extremely similar decomposition results which can be regarded approximately equal. However, we must note the surface scattering component is tinely higher (less than 1 dB) than the CTLR mode, and the dihedral scattering component is tinely lower (less than 1 dB) than the CTLR mode. The biggest difference lies in Trees* and Mountain*, where two compact-pol modes exactly have the inverse decomposition results for the surface and dihedral scattering as shown in bold type in Table 1. The above differences are from the α . In the $\pi/4$ mode, Eq. (17) can be rewritten as

$$\alpha = \frac{1}{2} \tan^{-1} \left(\frac{|t_{12}|}{0.5(t_{11} - t_{22} + t_{33}) - m_v} \right). \quad (19)$$

In the CTLR mode, the α can also be retrieved by the model-based target decomposition technique, and it can be expressed as

$$\alpha = \frac{1}{2} \tan^{-1} \left(\frac{|t_{12}|}{0.5(t_{11} - t_{22} + t_{33}) - t_{33}} \right). \quad (20)$$

The estimated m_v is less than t_{33} , which results in that α in (19) is smaller than (20), especially in the forest areas as shown in Figure 4. α of the $\pi/4$ mode is smaller than 45° , and can be clearly identified from the surrounding buildings area as shown in the rectangle box in Figure 4. However, α of the CTLR mode is larger than 45° and could not be distinguished from the neighbors. As a result, the $\pi/4$ mode raises the surface and decreases the dihedral scattering component with respect to the CTLR mode, and this difference demonstrably lies in the forest areas. From this point of view, the $\pi/4$ mode target decomposition is better than CTLR mode.

3.3 Comparison of the model-based decomposition and $m - \delta$ decomposition

In this section, we will make a comparison between the $\pi/4$ mode model-based target decomposition and the traditional $m - \delta$ decomposition.

The traditional $m - \delta$ target decomposition technique [7] is applied to obtain the three scattering mechanisms powers based on the degree of polarization (DoP) m , and the relative phase δ . The volume power is obtained via m . The residual power is split into two to represent the surface and dihedral

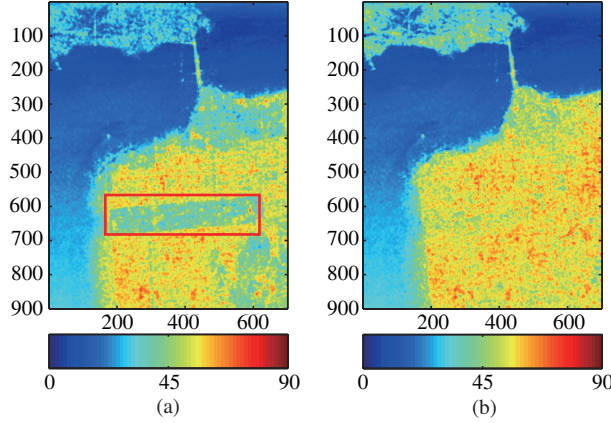


Figure 4 (Color online) Comparison of α in (a) the $\pi/4$ mode and (b) the CTLR mode ($^\circ$).

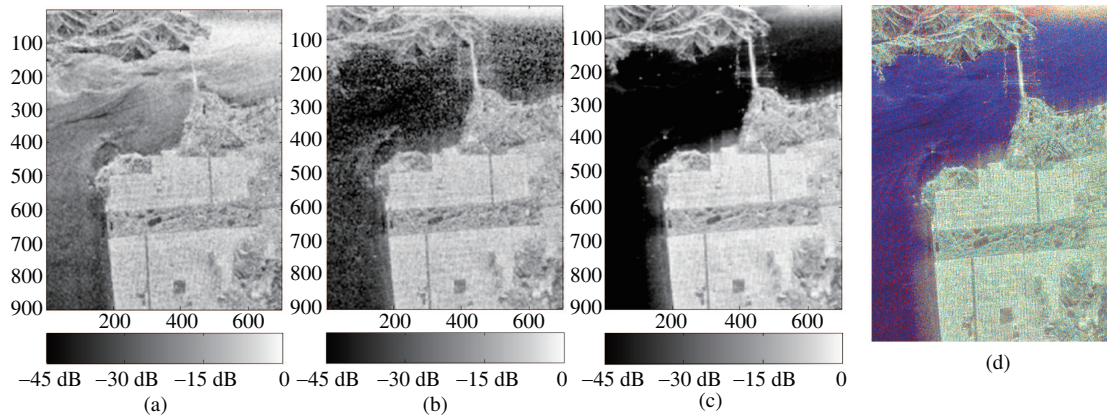


Figure 5 (Color online) The $m - \delta$ decomposition results: (a) surface scattering; (b) double-bounce scattering; (c) volume scattering; and (d) color coded image of this decomposition.

components using a geometrical factor $(1 \pm \sin \delta)$. The decomposition results of the three scattering mechanisms power and the reconstructed RGB coded image of the $m - \delta$ decomposition are shown in Figure 5. The statistical mean powers of typical targets are listed in Table 1. According to Figure 5(c), the volume scattering component estimated by $m - \delta$ decomposition is closely similar to that by the model-based decomposition. However, for the volume dominated areas (the forest and mountain), the volume scattering decreases more or less. For forest areas, the volume scattering decreases by 1 dB to -15.7 dB, and for mountain area, the volume decreases by 2 dB to -17.0 dB, which is not dominant again. For the ocean region, the surface and dihedral scattering components are not as accurate as the model-based decomposition results. As we can see in Figure 5(b), there are some strong and white pixels like noise which increase the dihedral scattering (-24.9 dB) and decreases the surface scattering (-18.7 dB). Due to this inaccuracy, some inconsistent dots appear in the ocean region as shown in Figure 5(d). For urban region, the surface scattering increases by about 2 dB to -12.8 dB and becomes dominant, while the dihedral scattering declines to -14.7 dB. For the forest and mountain areas, the volume scattering should be dominant, but via the $m - \delta$ decomposition, the volume scattering declines clearly. Due to all above accuracies, for the urban and the forest the RGB coding image cannot be shown as accurately and vividly as the model-based decomposition results. By contrast, we can conclude that the model-based decomposition technique is better than the $m - \delta$ decomposition.

4 Conclusion

In this paper, we retrieve the relation between the quad-pol coherence matrix and the Stokes parameters

of the $\pi/4$ mode compact polarimetry data. The Stokes vectors of the random volume scattering and rank-1 pure scattering mechanism are obtained. Further, the decomposition algorithm based on the compact-pol RVoG model is constructed. Based on this algorithm, we can obtain the power contributions of the three scattering mechanisms: surface, dihedral and volume scattering. The performance of the model-based target decomposition has been validated with L-band AIRSAR, San Francisco Bay.

We demonstrate the differences of the $\pi/4$ mode decomposition with respect to the CTLR mode. The $\pi/4$ mode decomposition raises surface scattering component and decreases dihedral scattering component with respect to CTLR mode. This inverse results are especially conspicuous in forest area. Further analysis of this will be made in the following research. In addition, we also make a comparison between the proposed decomposition and the $m-\delta$ decomposition. In comparison, the model-based decomposition can obtain better decomposition results.

Conflict of interest The authors declare that they have no conflict of interest.

References

- 1 Chen L. Investigation on models and methods of compact polarimetric SAR information processing. Dissertation for Ph.D. Degree. Beijing: Institute of Electronics, Chinese Academy of Sciences, 2013. 2–3
- 2 Souyris J C, Imbo P, Fjortoft R, et al. Compact polarimetry based on symmetry properties of geophysical media: the $\pi/4$ mode. *IEEE Trans Geosci Rem Sens*, 2005, 43: 634–646
- 3 Raney R. Hybrid-polarity sar architecture. *IEEE Trans Geosci Rem Sens*, 2007, 45: 3397–3404
- 4 Collins M J, Denbina M, Atteia G. On the reconstruction of quad-pol SAR data from compact polarimetry data for ocean target detection. *IEEE Trans Geosci Rem Sens*, 2013, 51: 591–600
- 5 Nord M, Ainsworth T, Lee J S, et al. Comparison of compact polarimetric synthetic aperture radar modes. *IEEE Trans Geosci Rem Sens*, 2009, 47: 174–188
- 6 Li H Y, Perrie W, He Y J, et al. Target detection on the ocean with the relative phase of compact polarimetry SAR. *IEEE Trans Geosci Rem Sens*, 2013, 51: 3299–3305
- 7 Charbonneau F J, Brisco B, Raney R K, et al. Compact polarimetry overview and applications assessment. *Can J Rem Sens*, 2010, 36, 298–315
- 8 Ballester-Berman J D, Lopez-Sanchez J M. Analysis on the potential of L-band polsar data for crop monitoring. In: *Proceedings of ESA Internal Workshop on POLInSAR*, Frascati, 2011
- 9 Lee J S, Pottier E. *Polarimetric Radar Imaging: From Basics to Applications*. Boca Raton: CRC Press, Taylor & Francis Group, 2009. 49–51
- 10 Raney R. Dual-polarized sar and stokes parameters. *IEEE Trans Geosci Rem Sens*, 2006, 3: 317–319
- 11 Freeman A, Durden S. A three-component scattering model for polarimetric sar data. *IEEE Trans Geosci Rem Sens*, 1998, 36: 963–973
- 12 Cloude S, Pottier E. A review of target decomposition theorems in radar polarimetry. *IEEE Trans Geosci Rem Sens*, 1996, 34: 498–518
- 13 Liu T, Huang G M, Wang X S, et al. Statistical assessment of H/A target decomposition theorems in radar polarimetry. *Sci China Inf Sci*, 2010, 53: 355–366
- 14 Cloude S. *Polarisation: Applications in Remote Sensing*. London: Oxford Univ Press, 2009, 142–158
- 15 Cloude S, Goodenough D, Chen H. Compact decomposition theory. *IEEE Geosci Rem Sens Lett*, 2012, 9: 28–32
- 16 López-Martínez C, Alonso-González A. Assessment and estimation of the RVoG model in polarimetric SAR interferometry. *IEEE Trans Geosci Rem Sens*, 2014, 52: 3091–3106
- 17 Huynen J R. Stokes matrix parameters and their interpretation in terms of physical target properties. In: *Proceedings of International Society for Optics and Photonics*, Orlando, 1990. 195–207